Section 1

Assimilation of atmospheric and land observations.

Data impact and sensitivity studies.

Methodological advances.

Application of Neural Networks to Speed Up Calculations of Radiation Parameterizations in the NOAA Global Ensemble Forecast System and Global Data Assimilation System ensembles

Alexei A. Belochitski[1] and Vladimir Krasnopolsky[2]

[1]IMSG@NOAA/NCEP/EMC, [2]NOAA/NCEP/EMC
Email: Vladimir.Krasnopolsky@noaa.gov

The NOAA Global Ensemble Forecast System (GEFS) and Global Data Assimilation System (GDAS) ensembles have been continually growing in complexity in order to provide forecasters with more accurate probabilistic forecast guidance and improve data assimilation to produce accurate initial conditions. Its demands for HPC resources perpetually outrun the increase in available computational power. For example, the operational GEFS v12 at its peak uses nearly the entirety of the NOAA WCOSS Dell Phase 3.5 supercomputer. Flexible and powerful numerical techniques are required to alleviate growing demands for HPC resources. The Neural network (NN) technique is increasingly being applied in NWP models to achieve this goal. NNs are used to accelerate calculations in NWP models and to develop faster and better constituents (parameterizations) of model physics at NOAA, ECMWF, UKMO, and other weather forecast centers.

The Environmental Modeling Center (EMC) of NCEP has extensive pioneering experience with the successful development of AI/ML applications for global atmospheric modeling, specifically for earlier versions of NCEP GFS and CFS (Krasnopolsky et al. 2010), as well as NCAR CAM. Several of the most time-consuming parts of model physics, including short wave radiation (SWR) and long wave radiation (LWR) parameterizations, have been emulated with high accuracy using an advanced and universal ML NN technique. Table 1 illustrates the performance gains that have been achieved. The speed up does not significantly decrease with increasing vertical resolution of the model.

	NCAR CAM (L=26)		NCEP CFS (L=64)	
	LWR	SWR	RRTMG LWR	RRTMG SWR
Speed up, *times*	150	20	16 (20)	60 (88)

Table 1 Speed up of LWR and SWR parameterizations achieved by using NN emulations in the NCAR CAM and NCEP CFS with different vertical resolutions (L). The presented numbers are for the 2010 versions of the models. Numbers in parentheses are speed-up factors for cloudy-sky conditions.

We showed that a comparable improvement in performance can be achieved in the latest version of GFS which constitutes the core of the GEFS (Belochitski and Krasnopolsky 2021). To assess the potential speed up, in the pilot study we configured a modern version of the GFS to run at the C384L64 (~25 km) configuration, the operational resolution of GEFS v12, and replaced the modern radiative transfer parameterizations (RRTMG) with their shallow NN-based emulators developed for this GFS. Table 2 shows an overall 23% speed up of the model, a result that is to a substantial degree due to an almost an order of magnitude acceleration of radiative transfer calculations.

	Speed up due to using NN emulator of radiation, *times*
Total	1.23
Radiation	9
Dynamical core	1.10

Table 2 Speed up of GFS model components due to the NN emulator of radiative transfer parameterizations in GFS pre-v16 at the GEFS operational resolution of C384L64.

An additional speed up stems from the fact that NN emulations provide a uniform computational efficiency across different atmospheric conditions, while the performance of the original physical parameterizations usually depends significantly on the local atmospheric state. For example, radiative transfer parameterizations take longer to complete their calculations under cloudy conditions, while performance of the NN emulation is invariant with respect to its inputs; therefore, NN emulations provide improved balancing and reduced idle time in an HPC parallel environment, as illustrated by the speed up of the dynamical core in Table 2. Such a speed up will allow us to increase the number of GEFS ensemble members from 30 to 38 and in GDAS from 80 to 98 without an increase in the amount of required computational resources.

Figure 1 illustrates accuracy of the NN emulators over a 10-day forecast. The development methodology for all stages of an NN-based emulation of the model physics components has been worked out and successfully tested. This methodology will be used in the current work with GEFS and GDAS. In a recent pilot study, we demonstrated that a single NN can accurately emulate both the LW and SW radiation parameterizations (RRTMG) in the new FV3 GFS. This development will provide an additional speed up in the calculation of atmospheric radiation.

NN emulators developed using the training software developed at NCEP are FORTRAN modules that are specifically designed for and are completely compatible with the NCEP's developmental and operational HPC environments.

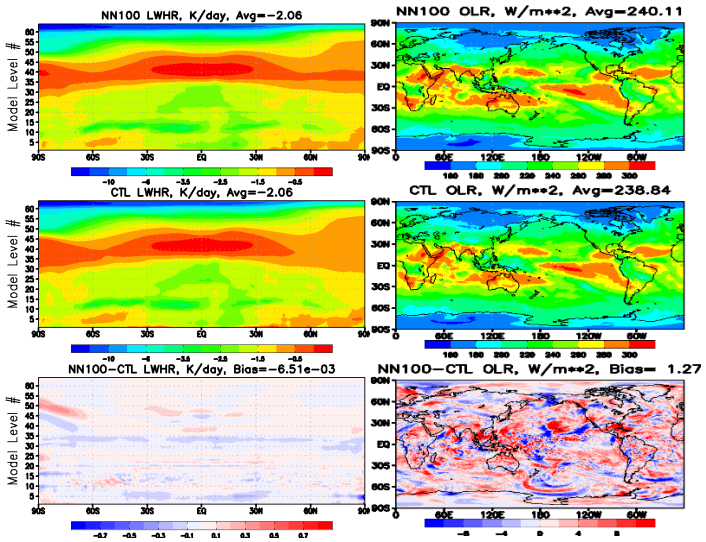

Figure 1 Results of parallel runs of GFS C384L64: time average over 10-day forecast. LWR heating rates (left column), and outgoing long wave radiation flux (right column). Upper row – results produced by NGFS (GFS with NN emulations of radiation parameterizations), medium – by GFS control (CTL) run, and the lower row the difference (NGFS – GFS). Vertical coordinate shows model level number.

References

Krasnopolsky, V. M., Fox-Rabinovitz, M. S., Hou, Y. T., Lord, S. J., & Belochitski, A. A. (2010). Accurate and Fast Neural Network Emulations of Model Radiation for the NCEP Coupled Climate Forecast System: Climate Simulations and Seasonal Predictions, *Monthly Weather Review*, 138, 1822-1842. doi: 10.1175/2009MWR3149.1

Belochitski, A. and V. Krasnopolsky (2021). Robustness of neural network emulations of radiative transfer parameterizations in a state-of-the-art general circulation model. *Geosci. Model Dev.*, 14, 7425–7437, 2021. https://doi.org/10.5194/gmd-14-7425-2021

Localization of satellite data

V.A.Gordin
123376, Russia. Email: vagordin@mail.ru
National Research University Higher School of Economics
Hydrometeorological Center of Russia, Moscow

When processing satellite information about various geophysical fields, it may be necessary to convert the fields of values averaged by pixels by satellite device into fields of local values on the output geographical grid. Sometimes it is necessary to inverse the transformation of the local values on the grid into a set of pixel integrals. Compact finite-difference schemes provide a higher accuracy order than classical explicit algorithms. In order to convert one type of field into another, it is sufficient to solve a system of linear algebraic equations (SLAE) with a sparse matrix. The transformations are not exact for an arbitrary field, and lead to errors that depend on the grid step and the wave spectrum of the interpolated fields. These errors for different algorithms are compared using the Fourier analysis. The comparison confirms the advantage of compact algorithms for a wide spectral range of waves. The advantage of the compact algorithms is also observed for Gaussian formulas, but in some special way. The grid knots for such formulae are not equidistantly spaced. Additional difficulties in converting one type of field to another exist in the vicinity of the boundary of the computational domain V. Modification of these algorithms is necessary here. For many geophysical problems, the spectral energy distribution of the interpolated fields is known *a priori* if these fields are interpreted as random. It is useful to apply this a priori information for interpolation to minimize the probabilistic error for a given type of field. Compact finite-difference schemes for these problems also provide minimal error.

Let's divide the area V into small squares (pixels) with a side h. Let N be the number of pixels at each coordinate. We use as input data the pixel-averaged values of a function $u(x,y)$ (e.g. temperature) $\{I_{j,k}\}_{j,k=1}^{N}$, where $I_{j,k}[u]=\int_{(j-1/2)h}^{(j+1/2)h}\int_{(k-1/2)h}^{(k+1/2)h} u(x,y)dxdy$ and evaluate the function u values $\{u_{jk}\}_{jk=0}^{n}$ in the grid's knots $\langle jh,kh\rangle$ (with the step h) that are in the pixels' centers. Let us determine by 2D Fourier transform $F_{y\to\eta}F_{x\to\omega}$ the symbol of the reference functional (of the integral by square pixel). Then we obtain:

$$\sigma_{reference}(\omega,\eta)=\frac{\sin(\omega h/2)\sin(\eta h/2)}{(\omega h/2)(\eta h/2)}. \quad (1)$$

We consider for the evaluation the nine-point stencils for both fields for creating a compact scheme. Let's shift the origin to the center of the square with coordinates $\langle j,k\rangle$ and use symmetry, with respect to the coordinate axes, and with respect to the diagonals:

$$aI_{0,0}+$$

$$b[I_{-1,0}+I_{0,-1}+I_{1,0}+I_{0,1}]/4+c[I_{-1,-1}+I_{1,-1}+I_{-1,1}+I_{1,1}]/4$$
$$=u(0,0)+p\left[u(0,-h)+u(0,h)+u(-h,0)+u(h,0)\right]+$$
$$+q\left[u(-h,-h)+u(-h,h)+u(h,-h)+u(h,h)\right]/4. \quad (2)$$

Let us determine 5 coefficients: *a, b, c, p, q.* We will assume that Eq. (2) is fulfilled on the monomial functions: $u=1, x^2, x^4, x^2y^2$ etc. To ensure the 4-th order of accuracy (in reality, the 5th due to the symmetry of scheme (2)), we need to use these 4 test functions, and to improve the order up to the 6-th we need to add x^6, x^4y^2. However, 5 coefficients in (2) are not sufficient for the goal, and we must limit ourselves to the 4th order. We obtain by substitution into compact relation (2) the following SLAE:

$$1\Rightarrow h^2(a+b+c)=1+p+q, \quad (3)$$
$$x^2\Rightarrow h^4(a+7b+13c)/12=h^2(2p+4q)/4,\quad x^4\Rightarrow$$
$$h^6\left[a+b(2+2\cdot 121)/4+c(4\cdot 121/4)\right]/80=h^4(2p+4q)/4,$$
$$x^2y^2\Rightarrow h^6\left[a+b(4\cdot 13)/4+c(4\cdot 169)/4\right]/144=h^4 4q/4.$$

To determine the local values of the function $u(x,y)$ by their mean values we need "global" SLAE (2). Its order is equal to the number of the grid knots. We need to modify equations (2) near the boundary of V.

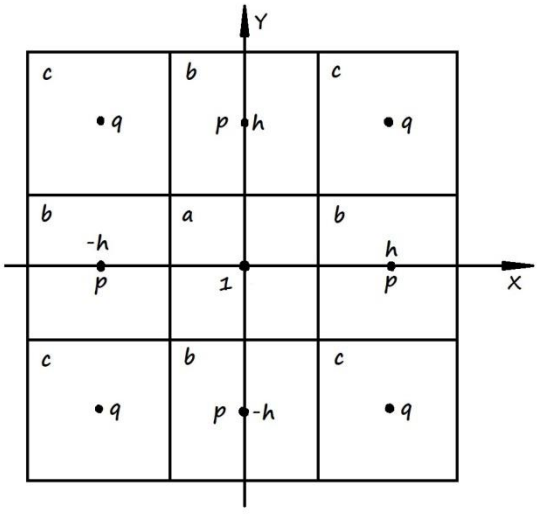

Fig.1. The weights for integrals by pixels and the coefficients for the values in knots in relation (2)

In each row of the matrix there is one element equal to 1, 4 elements with the value p and 4 with the value q. The remaining elements of the row are zero. If

p or q is also zero, then the matrix is sparser and it will be cheaper to solve SLAE (2). We obtain from "local" SLAE (3) the coefficients for "global" SLAE (2) for the normalization q=0:

$$a=\frac{247}{198h^2},\ b=\frac{31}{198h^2},\ c=\frac{-1}{72h^2},\ p=\frac{9}{44}.$$

The inequality $4|p|<1$ is fulfilled, and therefore (according to the Gershgorin theorem) the principal diagonal of the matrix dominates and the matrix of SLAE (2) is non-degenerate (if the boundary condition for the problem is suitable).

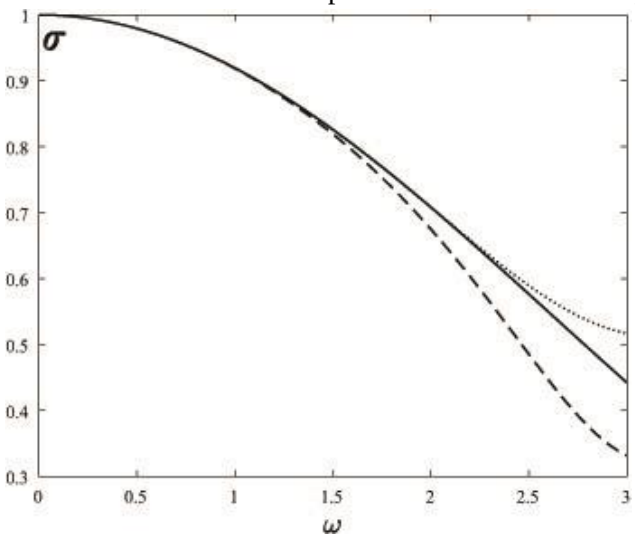

Fig.2. Solid line - symbol of the reference functional; dotted line - compact approximation for c=0; dashed line – for q=0. All the symbols are shown on the diagonal, i.e. when $\omega=\eta$.

Vice versa, if we determine the set of the integrals $\{I_{j,k}\}$, by the local values of the function, the normalization c=0 is preferable. We obtain the solution of SLAE (3):

$$a=\frac{258}{209h^2},\ b=\frac{102}{209h^2},\ p=\frac{140}{209},\ q=\frac{11}{209}.$$

The principal diagonal is dominant again, since $|a|>|b|$ here. The matrix of SLAE (2) is non-degenerate (if the boundary condition for the problem is suitable). The plots in Fig.2 confirm the high quality of the compact approximation for a wide wave range. The naive approximations (the integral is proportional to the average value of the function in the corners of the square): $I_{00}\approx h^2[u(-h/2,-h/2)+$

$$u(-h/2,h/2)+u(h/2,-h/2)+u(h/2,h/2)]/4 \quad (4)$$

and $u(0,0)=\alpha I_{0,0}+\beta\left[I_{0,-\mathrm{h}}+I_{0,\mathrm{h}}+I_{-h,0}+I_{\mathrm{h},0}\right]$, (5)

where $\alpha=5/\left(3h^2\right),\ \beta=-1/\left(6h^2\right)$. The corresponding symbols are shown in Fig.3, where the differences with the reference solution are much greater than in Fig.2.

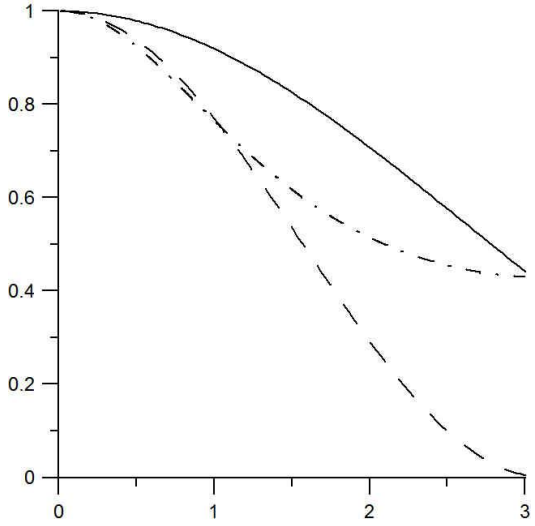

Fig.3. Symbols for the naive formulae. Solid line – ibid, dash dotted line – for formula (4), dashed line – for formula (5).

Thus, the compact formulae for the problems are much more accurate. The additional computation (the sparse matrix inversion) is not expensive.

Literature

D.Gayfulin, M.Tsyrulnikov, A.Uspensky. Assessment and Adaptive Correction of Observations in Atmospheric Sounding Channels of the Satellite Microwave Radiometer MTVZA-GY. Pure Appl. Geophys. V.175, PP.3653-3670, 2018.

Lele S.K. Compact finite difference schemes with spectral-like resolution. Journal of Computational Physics, 1992, V.103, №1, PP.16-42.

V.A.Gordin. Compact finite-difference scheme for differential relations' approximation. Mathematical Models and Computer Simulations. 2020 V.12, №2, PP.133-142.

Hairer E., Norsett S.P., Wanner G. Solving Ordinary Differential Equations. I. Non-stiff Problems. New York: Springer Verlag, 1993.

Operational Use of Shipborne GNSS-derived Precipitable Water Vapor in JMA's Mesoscale NWP System

HIGUCHI Mayuko
Numerical Prediction Development Center, Japan Meteorological Agency
E-mail: m-higuchi@met.kishou.go.jp

1. Introduction

The Japan Meteorological Agency (JMA) places high priority on improving accuracy in numerical weather prediction (NWP) for heavy rainfall.

Water vapor advection from seas in the lower atmosphere sometimes causes heavy rainfall, and NWP accuracy of heavy rainfall depends in good part on the precision of related fields as an initial condition. Although data assimilation is effective in improving initial field accuracy, water vapor observation networks for sea areas are not sufficient as those over land.

Ikuta et al. (2022) described improved prediction of heavy rainfall via assimilation of shipborne GNSS-derived precipitable water vapor (PWV) data (Shoji et al. 2017). Real-time PWV data from meteorological observation vessels for targeted areas and times also support operational NWP accuracy.

Against this background, JMA began assimilating shipborne PWV data in its mesoscale NWP system on August 31 2021. This report gives an overview of related experiments.

2. Shipborne PWV data and quality control

Shipborne PWVs are provided from two JMA observation vessels and four Japan Coast Guard vessels (as of March 2021) in near-real time.

Ground-based PWVs derived from the GNSS Earth Observation Network System (GEONET) of Geospatial Information Authority of Japan (analyzed from observation on the same principle as shipborne PWVs) have been used in mesoscale analysis since 2009 (Ishikawa 2010). Accordingly, equivalent quality control and data thinning are used for shipborne PWV data.

3. Assimilation experiments

Observing system experiments were conducted to evaluate the effects of shipborne PWV data assimilation on mesoscale analysis and forecasting. The control experiment (CNTL) had the same configuration as the operational JMA mesoscale NWP system as of May 2021, and the test experiment (TEST) was the same as CNTL except for the assimilation of shipborne PWVs. The experiments covered the period from June 1 to July 15 2021, which included several heavy rainfall events.

4. Shipborne PWV data quality

Figure 1 shows observation-minus-background (O-B) histograms of ground-based and shipborne PWVs. Table 1 presents mean and standard deviations of O-B and data counts of PWVs observed during the experimental period. The mean O-B of shipborne PWVs is slightly negative, while its absolute value is around the same as that of ground-based PWVs (approx. 10^{-1} mm). In Fig. 2's time sequence of shipborne PWV observation values, outliers are appropriately removed in gross error data rejection and other quality control processes.

5. Effects on analysis and forecasting

Several improved rainfall forecast cases were seen in TEST, as exemplified in the precipitation distribution of Fig. 3. Here, the initial condition water vapor field shows clear changes from assimilation of shipborne PWVs. The gradient PWV field gradient in the initial TEST condition is steeper near the shipborne PWV observation location (Fig. 4). Similar initial condition changes are seen in other improvements.

4. Summary

Shipborne PWV data quality is comparable to that of ground-based PWV data, and improved precipitation prediction from assimilation was observed. Excessive data rejection in quality control was seen in some cases, generally when there was a large discrepancy between the observed PWV and the NWP model's first-guess PWV. Further investigation on shipborne PWV usage and development for more appropriate quality control procedure are necessary toward the effective use of PWV data.

References

Shoji, Y., Sato, K., Yabuki, M., & Tsuda, T. (2017). Comparison of shipborne GNSS-derived precipitable water vapor with radiosonde in the western North Pacific and in the seas adjacent to Japan. Earth, Planets and Space, 69(1), 1-13.

Ikuta, Y., Seko, H., & Shoji, Y. (2022). Assimilation of shipborne precipitable water vapor by Global

Navigation Satellite Systems for extreme precipitation events. Quarterly Journal of the Royal Meteorological Society, 148(742), 57-75.

Ishikawa, Y. (2010). Data assimilation of GPS precipitable water vapor into the JMA mesoscale numerical weather prediction model. CAS/JSC WGNE Res. Act. Atmos. Ocea. Model, 40, 1-13.

Table 1. Shipborne and ground-based PWV: observations, mean values and standard deviations (Std) of O-B.

	Mean[mm]	Std[mm]	Number
ground-based PWV	0.29	2.50	1256145
shipborne PWV	-0.72	2.63	15562

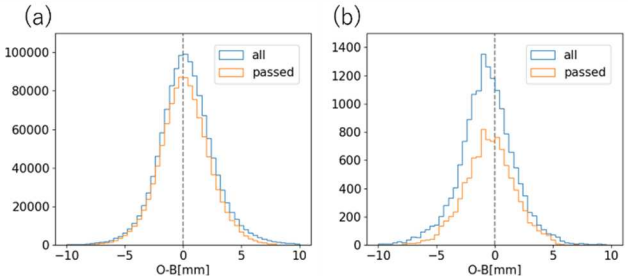

Figure 1. O-B histograms of (a) ground-based and (b) shipborne PWVs (blue: all data; orange: quality-controlled)

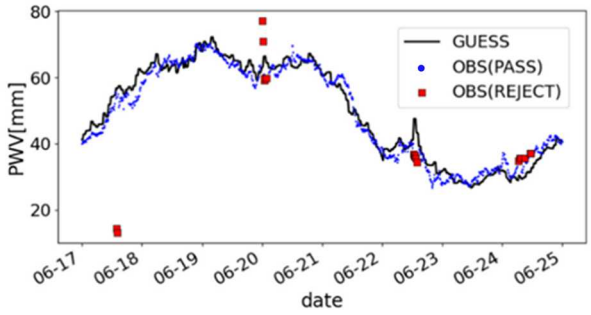

Figure 2. Ship-borne PWVs observed by JMA's Ryofu-maru vessel from 17 June to 25 June 2021 (black: background; blue: quality-controlled: red: rejected in quality control).

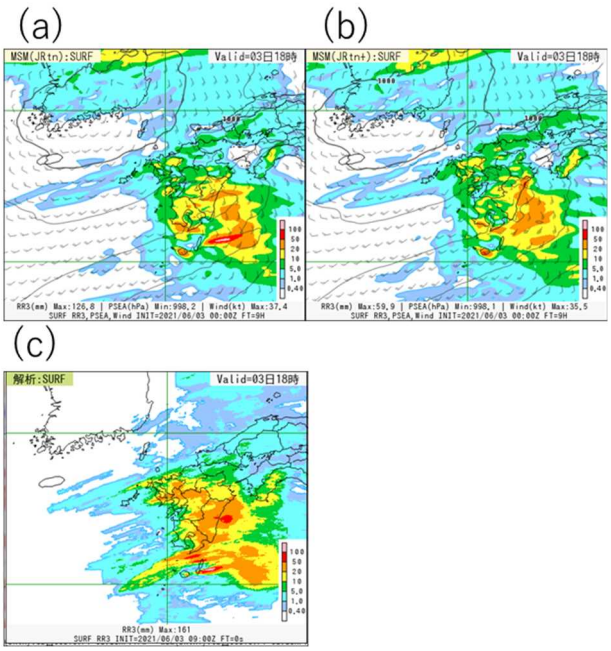

Figure 3. 3-hour accumulated precipitation at 09 UTC on June 3 2021. (a) TEST (9-hour forecast range), (b) CNTL (9-hour forecast range) (c) Radar rain-gauge analyzed precipitation.

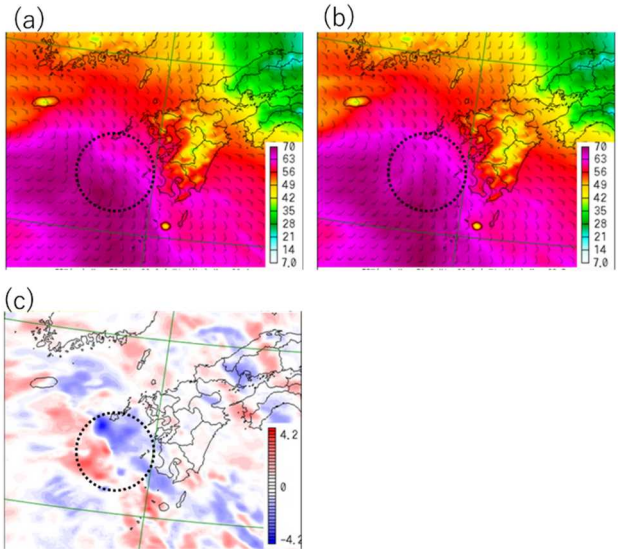

Figure 4. PWV in initial conditions at 00 UTC on June 3 2021. (a) TEST, (b) CNTL, (c) TEST-CNTL. Units are mm.

Implementation of New Bias Correction Method for Aircraft Temperature with Kalman Filter in JMA's Global NWP System

NAKAMURA Yuki
Numerical Prediction Development Center, Japan Meteorological Agency
E-mail: yuki.nakamura@met.kishou.go.jp

1. Introduction

The Japan Meteorological Agency (JMA) utilizes meteorological data collected by commercial aircraft for assimilation into its global NWP system (GSM), and previously introduced correction for biases known to exist in such data (Ballish et al. 2008) for appropriate application (Sako 2010). Here, bias correction values were created and updated once a month using statistics from the previous month on the temperature first-guess departure from JMA's global data assimilation system. This was done separately for each aircraft and each vertical level, and bias correction values were used to correct aircraft temperature data for the next month. However, this approach was problematic from the perspective of effective use of aircraft temperature observations. For instance, update frequency was insufficient and aircraft temperature data were used without bias correction if there were insufficient data to enable calculation of correction values. Accordingly, a new bias correction method designed to solve these problems was implemented into operation after determination of its effectiveness with the GSM.

2. New bias correction

Other NWP centers use variational correction to correct aircraft temperature bias (Zhu et al. 2015). As this exerts a high computational cost on JMA's NWP system, Kalman filtering is applied for correction at much lower cost. Bias correction values are updated at each analysis time (0000, 0600, 1200, 1800 UTC) and calculated for processing independent of analysis using a covariance of the first-guess departure separately for each aircraft, each vertical level and each flight phase (ascent, cruising and descent). Kalman filtering involves prediction and updating. In the prediction step, the estimated bias correction value $\widehat{\boldsymbol{\beta}}$, the covariance $\mathbf{P}$ and the covariance of the first-guess departure $\mathbf{D}$ are developed from time $k-1$ to time k as follows:

$$\widehat{\boldsymbol{\beta}}^{-}(k) = \widehat{\boldsymbol{\beta}}(k-1) \quad (1)$$

$$\mathbf{P}^{-}(k) = \mathbf{P}(k-1) + \mathbf{U} \quad (2)$$

$$\mathbf{D}^{-}(k) = \mathbf{D}(k-1) \quad (3)$$

The superscript "−" represents a priori estimation, and $\mathbf{U}$ is equivalent to the covariance of system noise. Subsequently, $\widehat{\boldsymbol{\beta}}$, $\mathbf{P}$ and $\mathbf{D}$ are updated using the average first-guess departure $\mathbf{b}$ for each analysis at the update step. The relevant formulas are shown below.

$$\widehat{\boldsymbol{\beta}}(k) = \widehat{\boldsymbol{\beta}}^{-}(k) + \mathbf{G}\left(\mathbf{b}(k) - \widehat{\boldsymbol{\beta}}^{-}(k)\right) \quad (4)$$

$$\mathbf{P}(k) = (\mathbf{I} - \mathbf{G})\mathbf{P}^{-}(k) \quad (5)$$

$$\mathbf{D}(k) = r\mathbf{D}^{-}(k) + (1-r)\left[\mathbf{b}(k) - \widehat{\boldsymbol{\beta}}^{-}(k)\right]^2 \quad (6)$$

$$\mathbf{G} = \frac{\mathbf{P}^{-}(k)}{\mathbf{P}^{-}(k) + \mathbf{D}(k)} \quad (7)$$

Here, $\mathbf{G}$ is the Kalman gain, r is the update ratio for $\mathbf{D}$, and $\mathbf{U}$ and r are unique values based on pre-runs of the new bias correction method. Evaluation using past observation and GSM data indicated that the new method enables calculation of more suitable bias correction values than the conventional approach (Figure 1).

3. Verification and results

To verify the influence of the new bias correction on the GSM, observing system experiments were performed as per the operational GSM on August 27 2020 (CNTL) and with the new bias correction method (TEST) for the experimental periods of August 2019 and January 2020. Initial bias correction values for TEST were created via Kalman filtering for the previous two years using first-guess departures.

The results indicated highly appropriate correction of aircraft temperature biases against first guesses with the new approach (Figure 2). Figure 3 (left) also shows that biases of aircraft temperature against first guesses were reduced. Biases of first-guess temperature against radiosonde observations were also reduced, especially around 250 hPa (Figure 3, right). Focusing on horizontal temperature distribution averaged over the experimental period, the temperature analysis field around 250 hPa in TEST was globally cooler than in CNTL (Figure 4). In terms of forecast accuracy, root mean squared errors of temperature and geopotential height against radiosondes and analysis were reduced in comparison with CNTL (Figure 5). The experimental results were consistent for both August 2019 and January 2020, and tropical cyclone track forecast error statistics were similar between TEST and CNTL. However, track forecast errors were improved for some tropical cyclones. These improvements are attributable to improved forecast accuracy of geopotential height in TEST.

As the new bias correction method demonstrated better performance than the conventional approach, it was implemented into JMA's global NWP system in June 2021.

References

Ballish, B. A., and K. Kumar, 2008: Systematic differences in aircraft and radiosonde temperatures. *Bull. Amer. Meteor. Soc.*, **89**, 1689-1708.

Sako, H., 2010: Assimilation of Aircraft Temperature Data in the JMA Global 4D-Var Data Assimilation System. *WGNE. Res. Activ. Earth. Sys. Modell.*, **40**, 1.33-1.34.

Zhu, Y., J. C. Derber, R. J. Purser, B. A. Ballish, and J. Whiting, 2015: Variational Correction of Aircraft Temperature Bias in the NCEP's GSI Analysis System. *Mon. Wea. Rev.*, **143**, 3774–3803.

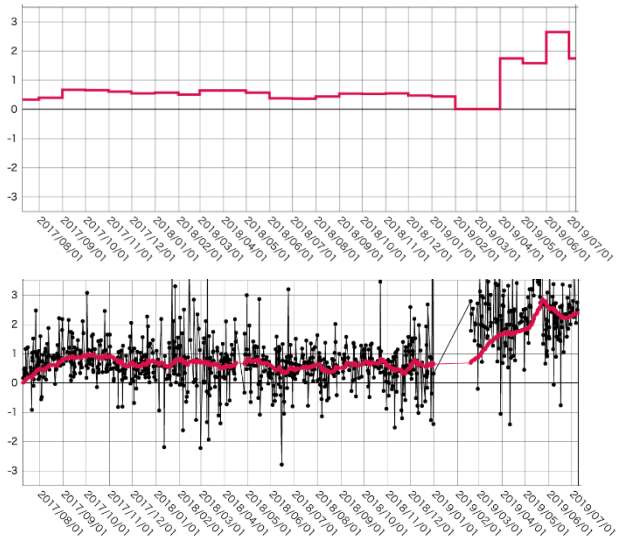

Figure 1. Time-series representation of bias correction values (red) for aircraft observation temperatures at around 200 hPa from July 10, 2017 to July 9, 2019. The top and bottom figures show values calculated using the conventional and new methods, respectively. The black line represents averaged first-guess departures at each analysis time. The unit is K.

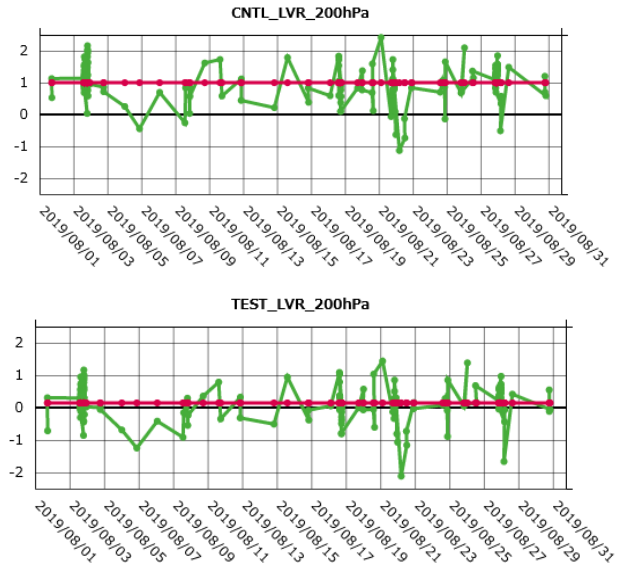

Figure 2. Time-series representation of first-guess departures of temperature [K] in aircraft observation around 200 hPa in August 2019. The green line represents first-guess departures at each analysis time, and the red line shows values averaged over the experimental period. The top and bottom figures show CNTL and TEST, respectively.

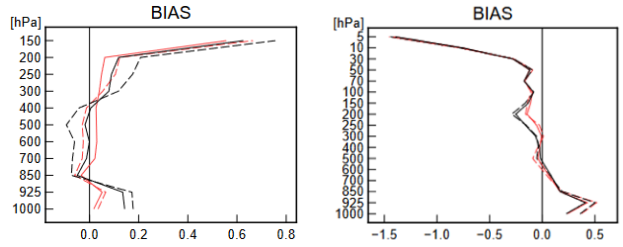

Figure 3. Temperature bias [K] in aircraft (left) and radiosonde (right) data against first guesses (dashed line) and analysis (solid line) at each vertical level for CNTL (black) and TEST (red) in August 2019. These biases were calculated only with data used in assimilation.

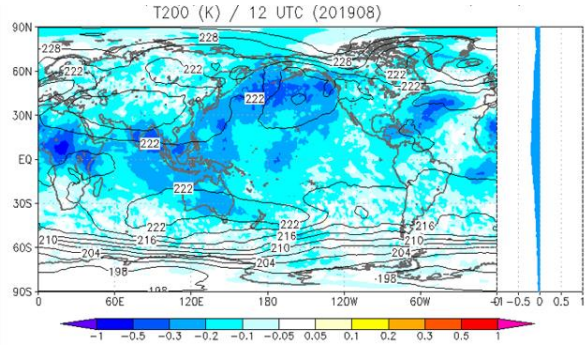

Figure 4. Average difference of horizontal temperature distribution at 200 hPa for the experimental period in August 2019 (only 1200 UTC) between TEST and CNTL. The zonal mean is also shown on the right. The unit is K.

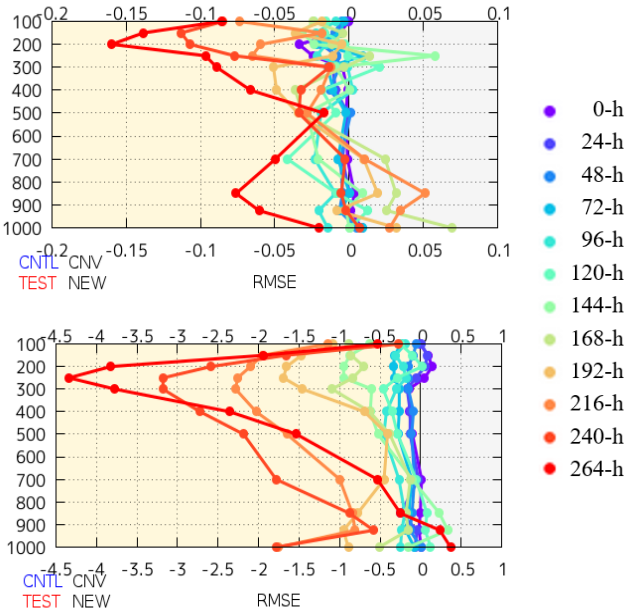

Figure 5. Differences in root mean square errors between TEST and CNTL against radiosondes averaged over the experimental period at each vertical level in the Northern Hemisphere in August 2019. The top and bottom figures show temperature [K] and geopotential height [m] forecasts, respectively, and colors represent each forecast time. The yellow area represents improvement because of reduced root mean square errors.

Operational Use of GOES-17 Atmospheric Motion Vectors (AMVs) in JMA's Global NWP System

NONAKA Kenichi
Numerical Prediction Development Center, Japan Meteorological Agency
E-mail: k-nonaka@met.kishou.go.jp

1. Introduction

Atmospheric Motion Vectors (AMVs) derived from geostationary meteorological satellites provide valuable information on tropospheric wind in the tropics and at mid-latitudes, and are used in data assimilation for JMA's global NWP system (GSM). GOES-17 is the second of the third-generation GOES series of satellites equipped with Advanced Baseline Imagers (ABIs), and began operation as GOES West at 137.2°W in Feb. 2019. GOES-16 is the same type of satellite, and is operated as GOES East at 75.2°W. GOES-16 AMVs have been operationally assimilated in the GSM since 29 July 2020 (Nonaka and Koyamatsu 2021).

This report presents the results of comparison between GOES-16 AMV and GOES-17 AMV data and related impacts on observing system experiments (OSEs) with GSM.

2. Comparison of GOES-16 and 17 AMVs

GOES-16 and 17 AMVs are derived from ABI sequential imagery using the same algorithm (Daniels et al. 2019), and their qualities are considered essentially comparable. The GOES-17 ABI has issues with its cooling system, and some degradation is observed in its infrared channel imagery over a period of several hours before and after the vernal and autumnal equinoxes (GOES-17 ABI Performance, n.d.). To determine the effects of the cooling issues on the quality of GOES-17 AMVs, the difference between these AMVs and those of GOES-16 was evaluated by comparing values collocated within 0.05-degree grid boxes.

Figure 1 shows statistical differences between GOES-16 and 17 infrared-channel (3.9 and 11.2 μm) AMVs (GOES-17 minus GOES-16) for speed and height every hour from 11 November 2019 to 25 October 2020. Although speed differences are relatively small, GOES-17 AMVs exhibited low height biases against GOES-16 AMVs for several hours a day during the period of approximately four months before and after the vernal and autumnal equinoxes at around 11 – 16 UTC in Feb., Apr., Aug. and Oct. The periods and hours during which GOES-17 AMVs exhibited height biases against GOES-16 AMVs correspond to those during which degradation is expected in GOES-17 ABI imagery. These results prompted avoidance of GOES-17 AMV data usage in the GSM for unreliable hours (11 to 16 UTC throughout the year). This is referred to here as time screening.

3. Optimization of QI threshold values

GOES-16 and 17 AMV data include a quality indicator without forecast testing (QI) (Holmlund 1998) which is used for data selection at major NWP centers. QI threshold values for both sets of AMVs were determined to reduce the bias and the standard deviation of observation minus background (O-B) statistics for the period from 10 July to 11 September 2020 using GSM as the background. Figure 2 shows typical QI dependency of O-B statistics for u-component of upper-layer (< 400 hPa) GOES-16 and 17 AMVs in the tropics (20°S –20°N). The bias and standard deviation tend to decrease as QI values increase.

4. Assimilation experiments

OSEs were performed with application of time screening to GOES-17 AMVs and new QI threshold values to both GOES-16 and 17 AMVs to determine impacts of assimilating GOES-17 AMV data on GSM. The experiments were based on an environment equivalent to that of JMA's operational system for September 2020, and were verified over one month around August 2020.

Figure 3 shows the zonal mean of relative improvement in root mean square errors (RMSEs) of wind vectors for 24-hour forecasts from 12 UTC initials using ERA5 data as a reference. Figures 3 (a) and (b) show results of applying a low QI threshold (QI > 60), and (b) shows those of applying time screening in addition. Figure 3 (c) shows results of applying a constant high QI threshold (QI > 87). It can be seen that the high QI threshold and time screening are effective in improving short-term wind forecast fields, especially in the troposphere from the tropics to the Southern Hemisphere.

5. Summary

Positive impacts were observed on analysis and short-term forecast fields in the troposphere

using GOES-17 AMVs in the GSM with application of time screening and the new optimal QI thresholds for GOES-16 and 17 AMVs. GOES-17 AMVs have been used operationally with the GSM since 29 June 2021.

References

Daniels, J., et al., 2019: GOES-R Advanced Baseline Imager (ABI) Algorithm Theoretical Basis Document For Derived Motion Winds, Version 3.1.

GOES-17 ABI Performance., accessed 1 May 2022, <https://www.goes-r.gov/users/GOES-17-ABI-Performance.html>.

Holmlund, K., 1998: The utilization of statistical properties of satellite-derived atmospheric motion vectors to derive quality indicators., Weather and Forecasting, Vol. 13, 1093-1104

Nonaka, K., and S., Koyamatsu, 2021: Operational Use of GOES-16 Atmospheric Motion Vector (AMV) and ScatSat-1/OSCAT Data in JMA's Global NWP System., WGNE Research Activities in Earth System Modelling, Rep. 51, 1.09-1.10.

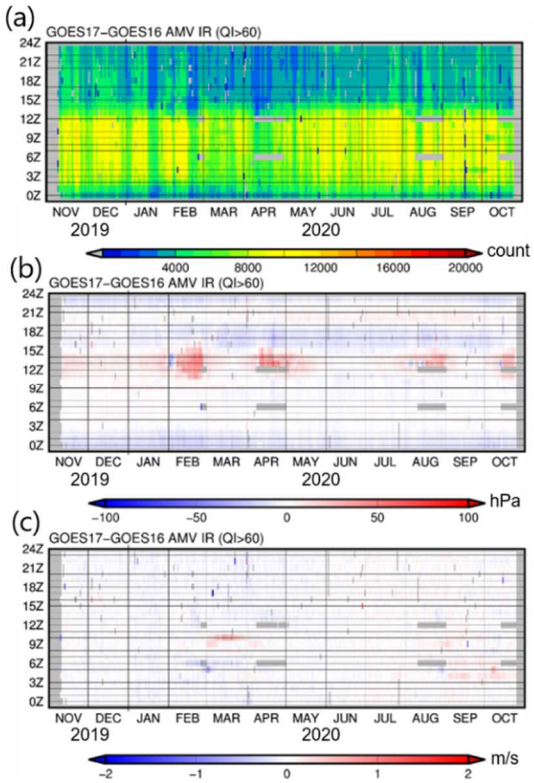

Figure 1. Time-series representation of statistical differences between GOES-16 and 17 infrared-channel AMVs every hour from 11 Nov. 2019 to 25 Oct. 2020. (a) Number of collocation vectors, (b) assignment height (pressure, hPa) difference (GOES-17 – GOES-16) and (c) speed difference (m/s) (GOES-17 – GOES-16). The horizontal and vertical axes represent the month and time (UTC), respectively.

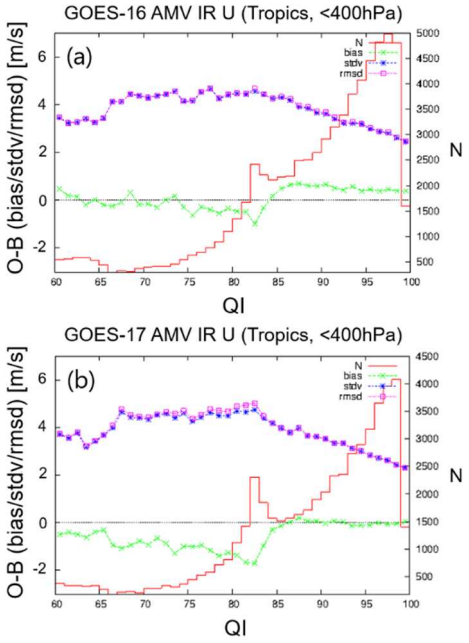

Figure 2. QI dependency of O-B bias, standard deviation and root mean square difference (RMSD) for upper-layer u-component wind in the tropics. (a) GOES-16 infrared–channel AMVs, and (b) GOES-17 infrared-channel AMVs. The red, green, blue and magenta lines indicate number of samples, bias, standard deviation and RMSD, respectively.

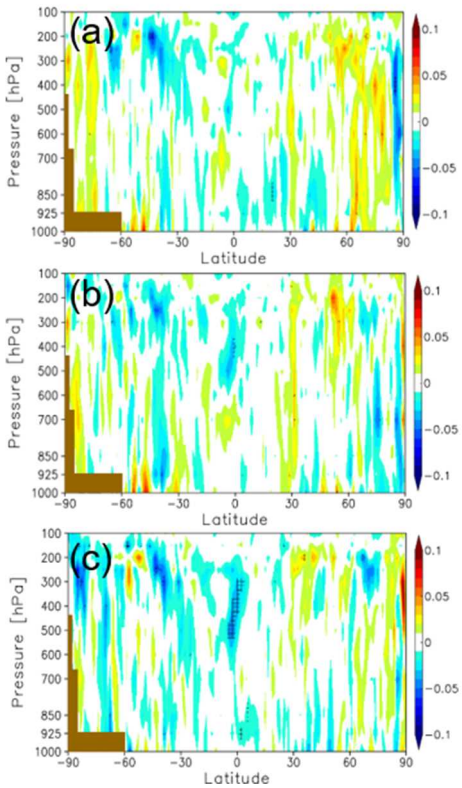

Figure 3. Zonal mean of relative improvement in root mean square error (RMSE) of wind vectors for 24-hour forecasts from 12 UTC initial against ERA5. The QI thresholds applied for GOES-16 and 17 AMVs are (a), (b) QI > 60 and (c) QI > 87. In (b) and (c), time screening is applied to GOES-17 AMVs. Negative values indicate reduced RMSEs from those of the reference experiment. Hatched areas represent statistically significant changes. The validation period is 1 – 31 August 2020.

Efficiency and Scaling of the Multigrid Beta Filter for Modeling Background Error Covariance

Miodrag Rancic, R. James Purser and Manuel Pondeca
IMSG at NOAA/NCEP/EMC
Email: miodrag.rancic@noaa.gov

1. Multigrid beta filter

A new technique for modeling of background error covariance, the Multigrid Beta Filter (MGBF), is under development at the Environmental Modeling Center - EMC (Purser et al. 2022). The new technique approximates a Gaussian using the Beta function with a finite support but achieves large spatial spread through the application of a multigrid technique. This combination results in a very efficient and easily parallelizable algorithm, which is expected to perform successfully on the large numbers of parallel processors of contemporary high-performance machines. In addition, the filter response can produce a large range of shapes of covariances, including those with negative side lobes, and even produce cross-correlations within the variational method, which was until now exclusive to ensemble-based methods.

The MGBF comes in two main flavors: a radial filter and a line filter. While the radial filter spreads the filter response within an ellipse of influence around the initial delta impulse, the line filter, like the recursive filters used in data assimilation at EMC until now, spreads this response along the selected lines. In the 2D case, three stages of filtering are needed; in the 3D case, seven stages are needed, with only six active filters at any generic grid point. The number of stages corresponds to the number of degrees of freedom in a general symmetric "aspect" tensor which controls the shape of the filter. In the isotropic case, where the x and y components of the 2D aspect tensor are equal, the line filters need only be applied in two dimensions, which provides a fast, isotropic version of the filter.

2. Tests with a standalone version of MGBF

A standalone version of the MGBF was developed to handle the same number of variables (six 3D and four 2D) as the recursive filter used in the GSI (EMC's operational data assimilation system). It operates at the same resolution as the GSI: 1792 x 1956 horizontal grid intervals and 50 vertical levels, but outside of the framework of the whole data assimilation system. It can therefore more speedily facilitate new developments, and the testing of different flavors of the filter.

Fig.1 shows the "speedup" achieved in a 2D+1D option of the radial and the line versions of the MGB filter, in a series of tests running on various constellations of processors (PEs), starting with 64 all the way up to 11264. Here, 2D+1D is a shorthand to describe the method where the 3D variables are filtered through the application of a horizontal 2D filter and a vertical 1D filter. Speedup is defined as inverse time – thus, on this graph, a higher value is better.

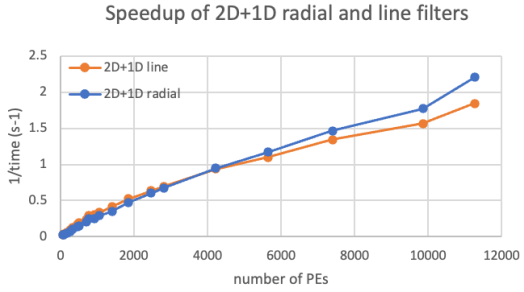

Figure 1 Speedup of the 2D+1D radial and line filters in the standalone version of the MGBF.

In this case, the line filter performs better up to about 2800 PEs, then the radial filter becomes faster thanks to the less frequent need to call the halo-exchange "side sending" subroutines. Development is already in progress for a new method which will group line filters into planar combinations to reduce the number of side-send halo exchanges and address this issue.

In the case of fully anisotropic 3D MGB filtering, the line version is systematically superior to the radial (Fig. 2), but its speedup with the increasing number of PEs still cannot match that of the isotropic 2D+1D version.

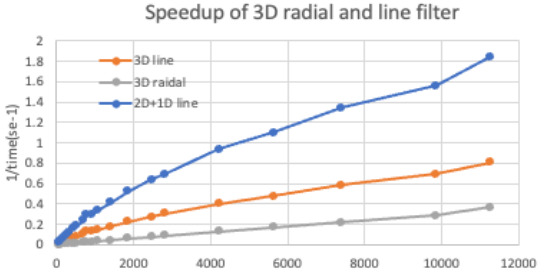

Figure 2 Speedup of the 3D radial and line filters in the standalone version of the MGBF.

Finally, we tested the "fast" isotropic version of the line filter (1D+1D+1D), which requires only two passes of the line filter horizontally (Fig. 3) and, as expected, it clearly has the best speedup rate.

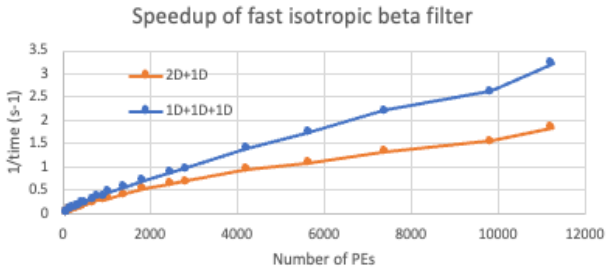

Figure 3 Speedup of the 1D+1D+1D line filter compared with the 2D+1D radial filter in the standalone version of the MGBF.

Note that the performance of all tested versions of the filter keeps improving all the way to 11264 PEs. A further increase in the number of PEs would require a substantial modification of the code to include halos over two rows of processors, which has not yet been done.

3. Tests with MGBF in GSI

We tested the isotropic version of the MGB line filter against the recursive filter (RF) in the GSI, using two different resolutions for the filter grid for the multigrid generation. The first configuration used the resolution of the analysis grid, and the second had about 10% lower horizontal resolution. Results are summarized in Figs. 4 and 5.

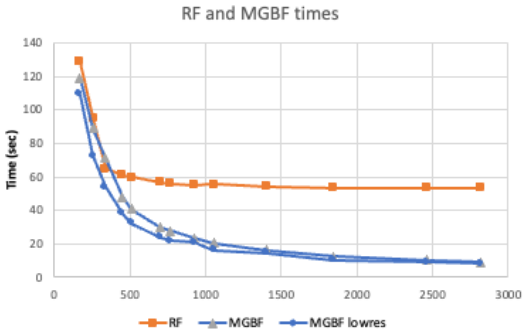

Figure 4 Times spent on filtering in runs of the GSI over various constellations of PEs. The isotropic version of the line MGBF is run at two different resolutions.

The isotropic version of the MGB line filter is about three times faster than the RF and scales much better (Fig. 4).

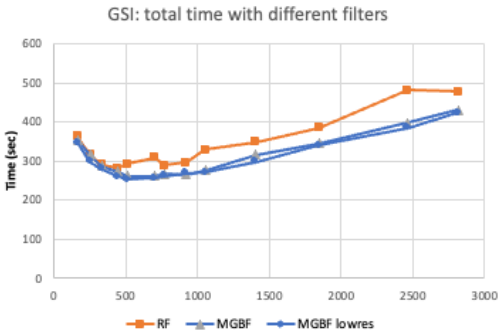

Figure 5 Total times spent on filtering in runs of the GSI over various constellations of PEs. The isotropic version of line MGBF is used, with two different resolutions.

Yet, though the total time spent in the GSI on filtering (Fig. 5) is systematically at least 20-25% lower with the MGBF than with the RF, the MGBF alone is not sufficient to push down the overall execution time of the GSI for processor numbers over ~600 PEs, presumably due to too many all-to-all communications and direct exchanges of data with disks. Therefore, some re-engineering of the GSI may be needed if we are to take full advantage of the new MGBF.

References

Purser, R. J., M. Rančić, M.S.F.V. De Pondeca, 2022: The Multigrid Beta function approach for modeling of background error covariance in the Real Time Mesoscale Analysis (RTMA), *Mon. Wea. Rev.,* **150,** (in press). https://doi.org/10.1175/MWR-D-20-0405.1

Effects of an Urban Canopy Scheme and Surface Observation Data on a Heavy Rain Event through Data Assimilation

SAWADA Ken[1], SEINO Naoko[2], KAWABATA Takuya[1] and SEKO Hiromu[1]
[1] *Meteorological Research Institute, Japan Meteorological Agency, Tsukuba, Japan*
[2] *Meteorological College, Kashiwa, Japan*
(e-mail: ksawada@mri-jma.go.jp)

1 Introduction

In order to improve the accuracy of forecasting localized heavy rainfall around urban areas, it is important to effectively utilize high frequent and high density surface observation data that have not been used for data assimilation so far. From the viewpoint of the data assimilation, the use of a forecast model that has the ability to accurately represent the city-specific heat island effect is required, to reduce the biases from observed data and to assimilate more observation data.

In this study, we incorporated a forecast model with an urban scheme into an ensemble-based assimilation system and assimilated dense surface data from Atmospheric Environmental Regional Observation System (AEROS, Soramame-Kun in Japanese nick name [1]), then, investigated how the use of the urban scheme and the surface data contributes to improve the reproducibility of the rainfall through numerical experiments for a heavy rain event in Tokyo metropolitan area on August 30, 2017.

2 Experiments and Results

We incorporated a forecast model (NHM) with a single-layered square prism urban canopy model (SPUC; Aoyagi and Seino 2011 [2]) as the urban scheme into a regional mesoscale assimilation system using the local ensemble transform Kalman filter (NHM-LETKF; Kunii 2014 [3]). Using this assimilation system, we conducted numerical experiments of a short-time heavy rainfall event that occurred in the Tokyo metropolitan area (Kanto) during the southward movement of an autumn rain front on August 30, 2017 (over 100 $\mathrm{mm\,h^{-1}}$ heavy rainfall for the vicinity of Nerima Ward, Tokyo, the location of which is indicated in Fig. 3). This analysis-forecast system has 200×200 horizontal grid points with 2 km resolution and the domain covers whole Kanto plain. The ensemble-size is 51 and the analysis-forecast cycle experiments start at 15 JST on August 28th with the analysis time interval of 3 hours. Almost as same as the observation data used in JMA's operational meso analysis system are assimilated. The settings of forecast model are the same as in Seino et al. 2018 [5].

The additional AEROS data (temperature, humidity, and wind speed) used in this study generally have a distribution as shown in Figure 1, although there are some differences depending on the assimilation time. We note that the temperature and humidity data within 2 m height and the wind speed data within 10 m height are used, by simple quality control method.

In the following, we refer to the analysis and forecast experiment using the conventional NHM-LETKF as CTRL, the NHM-LETKF experiment with SPUC as URB, and the URB experiment using the AEROS data for assimilation as URB_S.

SPUC scheme has the effects of increasing temperature of the lower troposphere mainly in the evening, developing the mixing layer and increasing the the amount of water vapor in the middle troposphere. It is also known that the rise in surface temperature is delayed in the morning. Figure 2 shows that the time series of temperature and wind speed at Nerima station are improved in URB. We can see that the initial temperature in URB is almost the same as the observation and the change of the wind speed in URB with the passage of the front (at 12 JST on August 30) is clearer than that in CTRL.

Figure 3 shows the one-hour accumulated precipitation in the forecasts from the initial data at 03 JST on August 30. In URB and URB_S experiments, the shape of the heavy rain area along with the local front becomes closer to that of observed (RA) than CTRL. We also note that the beginning of the construction of the heavy rainfall is getting earlier in URB and URB_S experiments. This implies that the improvement of the near surface temperature and wind fields by the use of SPUC scheme and AEROS data contributes to properly construct the convection which results in well reproduced heavy rain distribution.

3 Summary

The implementation of the urban scheme SPUC into the data assimilation system NHM-LETKF has improved the reproducibility of precipitation distribution in the localized heavy rainfall event on August 30, 2017. On the other hand, since AEROS is not specialized for capturing the atmospheric fields (Nishi et al. 2015 [4]), it is sometimes difficult to see a clear improvement in accuracy through its use. Thus, we need to continue to research and develop our system to make more effective use of the surface observations.

References

[1] AEROS, url= https://www.nies.go.jp/igreen/, urldate = 2022-05-01.

[2] T. Aoyagi and N. Seino. A square prism urban canopy scheme for the NHM and its evaluation on summer conditions in the Tokyo metropolitan area, Japan. *J. Appl. Meteor. Climtol.*, 50(7):1476–1496, 2011.

[3] M. Kunii. Mesoscale data assimilation for a local severe rainfall event with the NHM-LETKF system. *Weather and Forecasting*, 29(5):1093–1105, 2014.

[4] A. Nishi, K. Araki, K. Saito, T. Kawabata, and H. Seko. The consideration and application of the quality control method for the atmospheric environmental regional observation system (AEROS) meteorological observation data. *Tenki (in Japanese)*, 62(8):627–639, 2015.

[5] N. Seino, R. Oda, H. Sugawara, and T. Aoyagi. Observations and simulations of the mesoscale environment in TOMACS urban heavy rain events. *J. Meteor. Soc. Japan*, 96A:221–245, 2018.

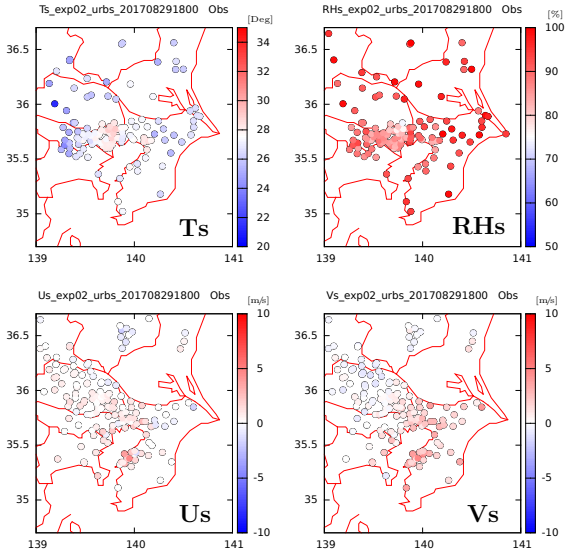

Figure 1: Distribution of the AEROS data used in the URB_S experiment at 03 JST on August 30.

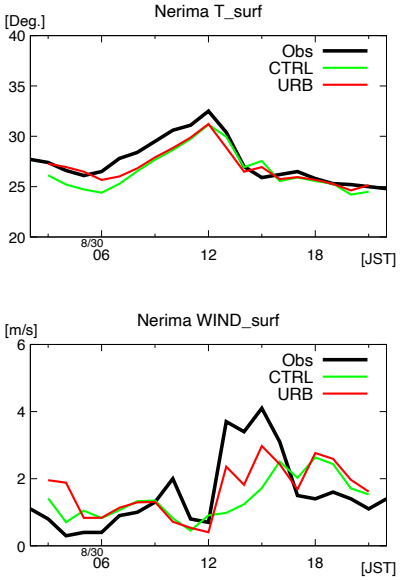

Figure 2: Time Series of surface temperature(upper) and wind speed(bottom) at Nerima observation station(AMeDAS).

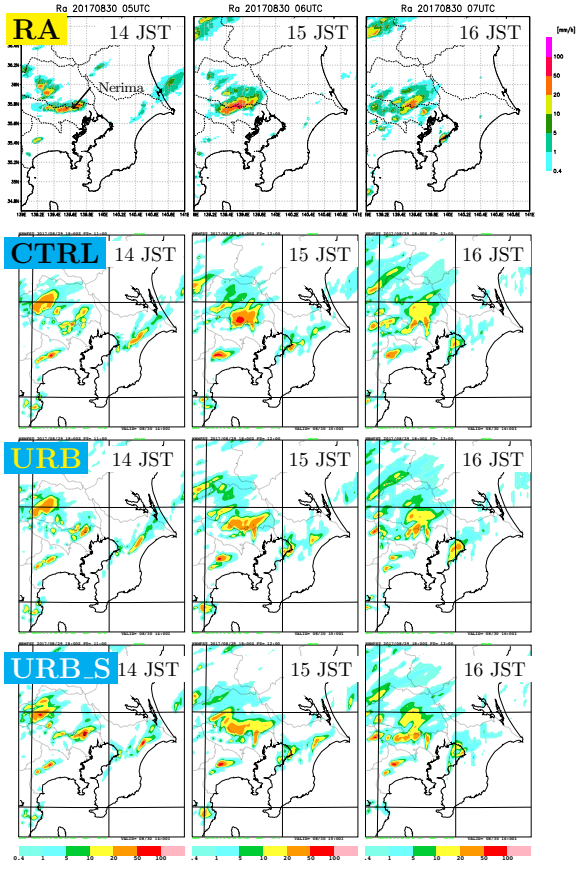

Figure 3: One-hour accumulated precipitation ([mm/h]; shaded as in the color bar) on August 30, 2017. The different panels show the radar/raingauge analyzed precipitation (RA) and the forecasts of CTRL, URB and URB_S.

Addition of microwave humidity sounder radiance data to all-sky assimilation in the JMA global NWP system

SHIMIZU Hiroyuki and KAZUMORI Masahiro
Numerical Prediction Development Center, Japan Meteorological Agency
E-mail:shimizu_h@met.kishou.go.jp

1. Introduction

It is more effective for the numerical weather prediction (NWP) to assimilate satellite microwave radiance data in all-sky condition than those in clear-sky condition. Accordingly, all-sky assimilation for microwave imagers and some microwave humidity sounders was implemented in JMA's global NWP system in December 2019 (Shimizu et al. 2020), thereby improving mid- and lower-tropospheric humidity forecasts and tropical cyclone track forecasts. In this context, JMA newly applied the all-sky assimilation scheme to the radiances around 183 GHz from Suomi-NPP, NOAA20/ATMS, DMSP-F17, F18/SSMIS and Megha-Tropiques/SAPHIR. In addition, assimilation of radiances from FY-3C/MWHS-2 for all-sky conditions was also commenced. These developments were implemented into JMA's operational global NWP system in June 2021. This report summarizes these developments and their impacts on forecasting.

2. Quality control updates

Observation error assignment is based on the symmetric (average of observation and first guess (FG)) cloud amount (Geer and Bauer 2011). As a measure of this, an index depending on available channels for each sensor is derived as follows:

(1) If brightness temperatures (TB) at 90 GHz (TB_{90}) and 150 GHz (TB_{150}) are available (Suomi-NPP, NOAA-20/ATMS, DMSP-F17/SSMIS, and FY-3C/MWHS-2), a scattering index (SI) (Geer et al. 2014) is used, defined as

$$SI = (TB_{90} - TB_{150}) - (TB_{90}^{clr} - TB_{150}^{clr})$$

Here, the superscript *clr* indicates the calculated TB under the assumption of clear-sky conditions.

(2) If the TB of DMSP-F18/SSMIS at 150 GHz is unavailable due to malfunction, an alternative index defined as C_{37} (Geer and Bauer 2011) is used:

$$C_{37} = 1 - \frac{TB_{37v} - TB_{37h}}{TB_{37v}^{clr} - TB_{37h}^{clr}}$$

Here, TB_{37v} represents the vertically polarized TB at 37 GHz, and TB_{37h} represents the horizontally polarized value.

(3) For Megha-Tropiques/SAPHIR, which has none of the above channels, the index C_{183} using the TB at lowest peaking channel 6 (183 ± 11 GHz) (TB_{ch6}) is used (Chambon and Geer 2017):

$$C_{183} = TB_{ch6}^{clr} - TB_{ch6}$$

Minor changes are applied in the quality control update. To expand microwave humidity sounder coverage over land, radiances of DMSP-F17/SSMIS and Megha-Tropiques/SAPHIR are assimilated, when the radiances are less sensitive to the surface. Exclusive thinning between SSMIS and MHS is removed.

The addition of all-sky microwave humidity sounders and the above updates significantly increases the number of assimilated microwave humidity sounder data (Figure 1).

3. Impact evaluation: data assimilation experiments

The impact of adding all-sky microwave humidity sounders and quality control updates was evaluated in data assimilation experiments with JMA's global NWP system. The experiment period for boreal winter was from 10 December 2019 to 11 February 2020, and boreal summer was from 10 July to 11 September 2019. The CNTL experiment had the same configuration as JMA's operational global NWP system as of October 2020, and the TEST experiment was performed with the updates described in Section 2 in addition to the CNTL experiment conditions.

Figure 2 shows changes in the standard deviation of FG departures against CNTL. The FGs of TEST were closer to observations than those of CNTL for clear-sky radiance (CSR) data, which are sensitive to humidity in the mid- to upper-troposphere (Fig. 2a) and for radiosonde relative humidity (Fig. 2c). These results indicate that short-range forecasting of mid- to upper-tropospheric humidity fields was improved consistently against observations. The FGs of TEST were also closer to observations of the CrIS (Fig. 2b) and aircraft wind observations (not shown). These outcomes indicate that all-sky assimilation for humidity sounders also has positive impacts on temperature and wind fields due to the tracing effect of 4D-var (Geer et al. 2014). Figure 3 shows zonal mean improvement ratios in root mean square errors against ECMWF analysis for specific humidity and temperature. In the troposphere, humidity and temperature field were improved (Fig. 3), and this improvement was

retained up to two forecast days (not shown).

4. Summary

Addition of microwave humidity sounders (Suomi-NPP, NOAA20/ATMS, DMSP-F17, F18/SSMIS, Megha-Tropiques/SAPHIR, and FY-3C/MWHS-2) to all-sky assimilation was implemented into JMA's global NWP system in June 2021. Related experiments showed a positive impact on the accuracy of FGs for tropospheric humidity and temperature fields. The forecast fields of humidity and temperature were improved and these were retained up to two forecast days.

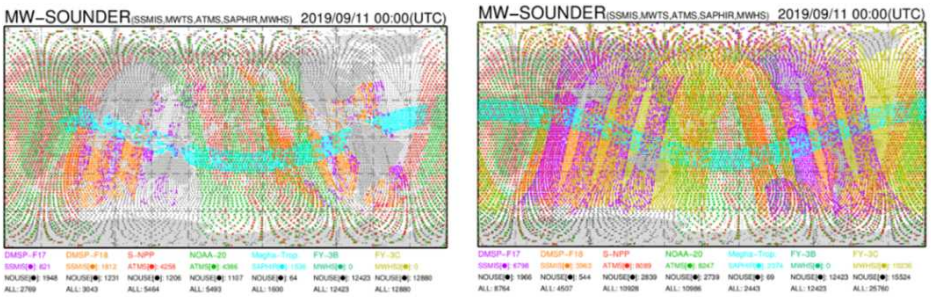

Figure 1: Coverage of microwave humidity sounder data assimilated during the 00 UTC time window on 11 September 2019. Left: before updates; right: after.

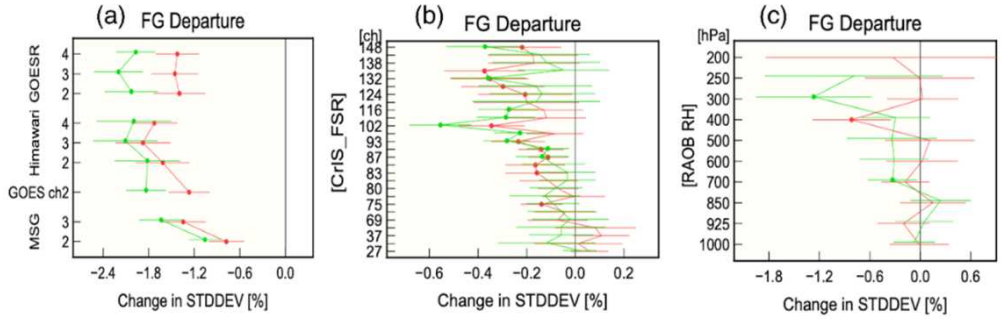

Figure 2: Normalized changes in standard deviation for FG departures in (a) CSR radiances from operational geostationary satellites, (b) CrIS radiances, and (c) radiosonde humidity. Horizontal lines show confidence levels of 95%. The validation periods are from 20 July to 11 September 2019 (red lines) and from 21 December 2019 to 11 February 2020 (green lines).

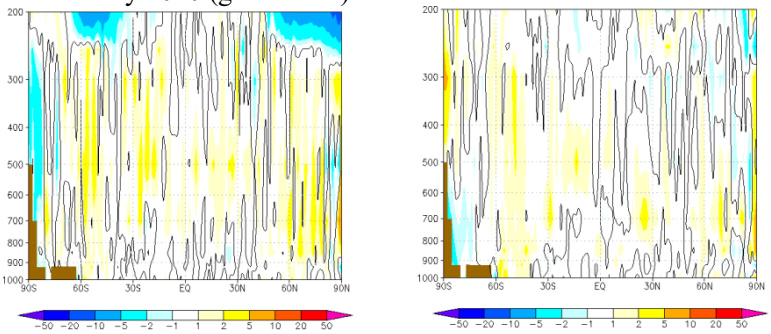

Figure 3: Zonal mean of relative improvement ratio [%] in root mean square errors against ECMWF analysis for day 1 forecasts of specific humidity (left) and temperature (right). Warm and cool colors represent improvement and degradation of TEST values, respectively. The verification period is 1 month (August 2020).

References

Chambon, Philippe and Alan J. Geer. (2017). All-sky assimilation of Megha-Tropiques/SAPHIR radiances in ECMWF numerical weather prediction system. *ECMWF Tech. Memo*., **802**.

Geer, A. J., Baordo, F., Bormann, N. and English, S. (2014). All-sky assimilation of microwave humidity sounders. *ECMWF Tech. Memo*., **741**.

Geer, A. J. and Bauer, P. (2011). Observation errors in all-sky data assimilation. *Quart. J. Roy. Meteor. Soc*., **137**, 2024-2037.

Shimizu, H., M. Kazumori and T. Kadowaki. (2020). Implementation of all-sky microwave radiance assimilation into JMA's global NWP system. *WGNE. Res. Activ. Earth. Sys. Modell*., **50**, *WCRP Report No.12/2020. WMO, Geneva,* 1.21-1.22.

Implementation of hybrid 3DVar in JMA's local analysis

YOKOTA Sho, BANNO Takahiro, OIGAWA Masanori, AKIMOTO Ginga,
*KAWANO Kohei, IKUTA Yasutaka
Japan Meteorological Agency
(email: k_kawano@met.kishou.go.jp)

1. Introduction

Three-dimensional variational data assimilation (3DVar) with 5-km horizontal grid intervals are used in JMA's local analysis (LA) to create initial atmospheric analysis fields in local forecast model with 2-km horizontal grid intervals (Ikuta et al. 2021). In the assimilation reported here, the horizontally homogeneous and isotropic climatological background error covariance $\mathbf{B}_c$ is used (as of February 2022) for the background error covariance of the first guess, and the flow-dependent error covariance ($\mathbf{B}_e$) is not used. However, it is possible to implement hybrid 3DVar (Lorenc 2003) with the weighted average of $\mathbf{B}_c$ and $\mathbf{B}_e$ as the background error covariance, estimating $\mathbf{B}_e$ from the ensemble perturbations of the mesoscale ensemble prediction system (MEPS, Ono et al. 2021), as applied by JMA. This report outlines hybrid 3DVar implementation in LA and related effects.

2. Hybrid 3DVar formulation

In hybrid 3DVar, the analysis increment $\delta\mathbf{x}$ is determined by minimizing the cost function

$$J(\mathbf{v}) = \frac{1}{2}\mathbf{v}^T\mathbf{v} + \frac{1}{2}(\mathbf{H}\delta\mathbf{x} - \mathbf{d})^T\mathbf{R}^{-1}(\mathbf{H}\delta\mathbf{x} - \mathbf{d}) + J_{bc},$$

$$\delta\mathbf{x} \equiv \mathbf{B}^{1/2}\mathbf{v} \equiv \begin{bmatrix}\beta_c\mathbf{B}_c^{1/2} & \beta_e\mathbf{B}_e^{1/2}\end{bmatrix}\begin{bmatrix}\mathbf{v}_c \\ \mathbf{v}_e\end{bmatrix},$$

where $\mathbf{v} = [\mathbf{v}_c{}^T, \mathbf{v}_e{}^T]^T$ is a control vector, $\mathbf{d} = \mathbf{y}^o - H(\mathbf{x}^b)$ is the difference in observation $\mathbf{y}^o$ from the first guess $\mathbf{x}^b$, H and $\mathbf{H}$ are the observation operator and the related tangent linear version, $\mathbf{R}$ is the observation error covariance, and J_{bc} is a bias correction term. β_c and β_e are weights for the hybrid covariance, set as $(\beta_c^2, \beta_e^2) = (0.5, 0.5)$.

$\mathbf{B}_e$ is created from 100 ensemble perturbations using 5 lagged average forecasts (LAF) of MEPS with 20 members and spatial localizations with Gaussian functions (scales of $1/\sqrt{e}$ are set as 100 km horizontally and 0.5 km vertically) to reduce sampling errors. $\mathbf{B}_e$ is inflated by multiplying the factor, which is the ratio of $\mathbf{B}_c$ and the horizontal mean of $\mathbf{B}_e$ for potential temperature at 5.5 km above ground level, meaning that error variance is comparable to the magnitude of $\mathbf{B}_c$.

3. Verification

To verify the effects of hybrid 3DVar implementation, sensitivity experiments were conducted in 3-hour blocks for 2 – 15 July 2020 based on the CNTL experiment utilizing the configuration of JMA's operational local NWP system as of May 2021, with $\mathbf{B}_c$ updated using National Meteorological Center method (Parrish and Derber 1992). Here, sensitivity experiments with 20 and 100 ensemble perturbations (1 and 5 LAF, respectively) are referred to as M020 and M100, respectively.

In M020 and M100 root mean square errors in forecasts were smaller than those in CNTL,

especially for surface temperature, specific humidity and horizontal wind (not shown). The equitable threat score (ETS) for precipitation was better in M020 and M100 than that in CNTL, especially with thresholds over 5 mm/h (Fig. 1). These improvements were greater in M100. In forecasts from analysis at 12 UTC on 3 July, the position of predicted heavy rain in M100 was closer to observation than M020 and CNTL (Fig. 2), which may relate to the flow-dependent analysis increment of low-level variables. Associated improvements were also observed in the boreal winter experiment for 11 – 21 January 2020 (not shown).

4. **Summary**

The implementation of hybrid 3DVar utilizing 100 ensemble perturbations of MEPS in LA improved forecasting of precipitation and surface variables. The update was applied to JMA's operational system in March 2022.

References

Ikuta, Y., T. Fujita, Y. Ota, and Y. Honda., 2021: Variational data assimilation system for operational regional models at Japan Meteorological Agency, J. Meteor. Soc. Japan, 99(6), 1563−1592.

Lorenc, A. C., 2003. The potential of the ensemble Kalman filter for NWP: a comparison with 4D-Var. Quart. J. Roy. Meteor. Soc., 129, 3183–3203.

Ono, K., M. Kunii, and Y. Honda, 2021: The regional model-based Mesoscale Ensemble Prediction System, MEPS, at the Japan Meteorological Agency. Quart. J. Roy. Meteor. Soc., 147, 465–484.

Parrish, D. F., and J. C. Derber, 1992: The National Meteorological Center's spectral statistical-interpolation analysis system. Mon. Wea. Rev., 120(8), 1747–1763.

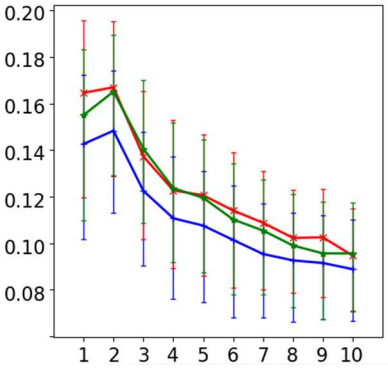

Figure 1. Equitable threat score for precipitation with a 10 mm/h threshold (vertical axis) at each forecast time [hours] (horizontal axis) in experiments for 2 – 15 July 2020 compared with JMA radar/raingauge analyzed precipitation (blue: CNTL; green: M020; red: M100). Error bars show 95% confidence intervals.

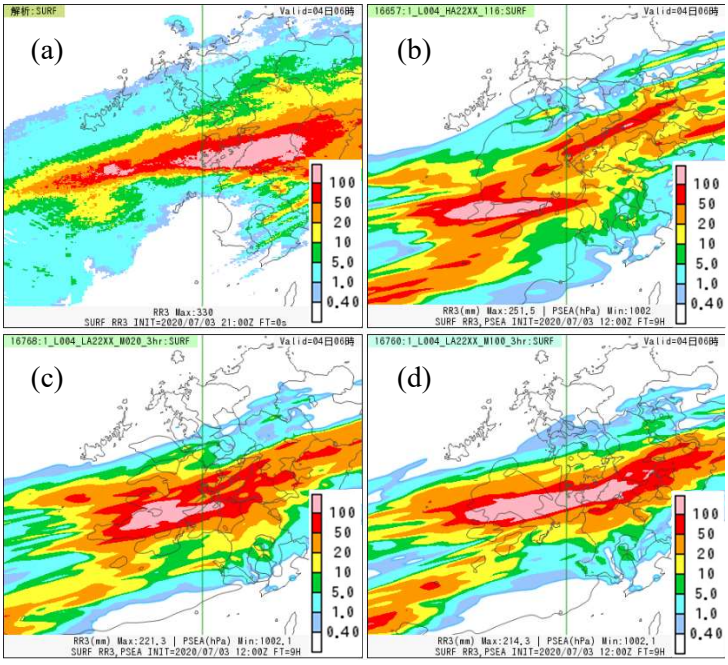

Figure 2. Three-hour precipitation (mm) for 18 – 21 UTC on 3 July 2020 in predictions from 12 UTC (a: JMA radar/raingauge analyzed precipitation; b: CNTL; c: M020; d: M100).